ISSN 0001-4338, Izvestiya, Atmospheric and Oceanic Physics, 2020, Vol. 56, No. 9, pp. 916–926. © Pleiades Publishing, Ltd., 2020.
Russian Text © The Author(s), 2019, published in Issledovanie Zemli iz Kosmosa, 2019, No. 4, pp. 3–17.

PHYSICAL BASES AND METHODS OF STUDYING THE EARTH FROM SPACE

Application of Radar Polarimetry to Monitor Changes in Backscattering Mechanisms in Landslide Zones Using the Example of the Collapse of the Bureya River Bank

V. G. Bondur[a, *], **T. N. Chimitdorzhiev**[b, **], **A. V. Dmitriev**[b], **P. N. Dagurov**[b], **A. I. Zakharov**[c], **and L. N. Zakharova**[c, ***]

[a]*AEROCOSMOS Research Institute for Aerospace Monitoring, Moscow, Russia*
[b]*Institute of Physical Materials Science, Siberian Branch, Russian Academy of Sciences, Ulan-Ude, Russia*
[c]*Kotelnikov Institute of Radioengineering and Electronics, Russian Academy of Sciences, Fryazino Branch, Fryazino, Russia*
**e-mail: vgbondur@aerocosmos.info*
***e-mail: tchimit@gmail.com*
****e-mail: ludmila@sunclass.ire.rssi.ru*

Received July 17, 2019; revised July 19, 2019; accepted July 22, 2019

Abstract—Possibilities of using radar polarimetry methods for identifying landslide zones are analyzed. The transformation of the dominant mechanism of signal scattering by the reflecting surface was used as a key feature of landslide zones. The polarimetric data from the PALSAR-2 radar of the ALOS-2 satellite are processed using the Freeman—Durden and Cloude—Pottier decompositions at four test sites selected in the region of the landslide caused by the collapse of the bank of the Bureya River. It is found that the results of decompositions are consistent with each other; however, in some areas there are significant differences due to the specific features of the basic model assumptions. It is shown that, before the descent of the landslide masses, three main mechanisms of radar signal scattering existed in the analyzed region: single surface, volumetric, and double scattering. After the collapse, this area was dominated by single scattering characteristic of the reflective surface with large-scale irregularities free of vegetation, due to which the landslide descent zone can be confidently recognized. The significant potential of using radar polarimetry for remote diagnostics of the consequences of landslide phenomena has been demonstrated.

Keywords: remote sensing, radar polarimetry, landslide, radar scattering mechanisms, decomposition of polarimetric signals

DOI: 10.1134/S0001433820090054

INTRODUCTION

Space methods and instruments are widely used to monitor various natural disasters such as earthquakes (Akopyan et al., 2017; Bondur and Zverev, 2005, 2007; Bondur and Smirnov, 2005; Bondur et al., 2007, 2010, 2016a, 2016b), landslides (Zakharov et al., 2018; Zakharov and Zakharova, 2019; Zakharova et al., 2019; Bondur et al., 2019; Mikhailov et al., 2014; Shirzaei et al., 2017), typhoons (Bondur et al., 2008a, 2008b, 2009), and others (Bondur et al., 2009, 2010, 2012). Synthetic-aperture radars (SAR) are among the most promising means of Earth remote sensing (ERS) from space (Verba et al., 2010; Bondur and Chimitdorzhiev, 2008a, 2008b, 2019; Bondur and Starchenkov, 2001; Bondur, 2011; Dmitriev et al., 2014; Zakharov et al., 2012; Chimitdorzhiev et al., 2016). The advantage of radar sensing is independence of the image acquisition process from the illumination of the captured surface and the presence of clouds. This issue makes it possible to carry out the radar monitoring of emergency situations (Bondur et al., 2009, 2012), including landslides (Zakharov et al., 2018; Mikhailov et al., 2014; Shirzaei et al., 2017), floods (Dubina et al., 2018), the consequences of tsunamis (Watanabe et al., 2016), etc. Landslide monitoring is an important field of applying polarimetric remote sensing methods (Zakharov et al., 2019; Zakharova et al., 2019; Bondur et al., 2019; Czuchlewski et al., 2003; Yonezawa et al., 2012; Shimada et al., 2014; Li et al., 2014a, 2014b; Luo et al., 2016; Shibayama et al., 2015; Watanabe et al., 2016).

This paper analyzes the capabilities of radar polarimetry methods for assessing changes in the reflective properties of the Earth's surface using the example of a landslide that occurred in December 2018 on the Bureya River. The first information about the large-scale descent of landslide masses that occurred on December 11, 2018, was obtained from the images of the Sentinel-2B optical sensor and the Himawari-8 multispectral scanner (thermal imager) (Kramareva et al., 2018). It was found that the area of the landslide zone, together with the ridge in the river bed, was about 0.4 km^2; the approximate time of ground descent into the river was 4:30 GMT on December 11, 2018. An analysis of the Bureya landslide by the method of radar interferometry based on data from the Sentinel-1 radar was carried out in (Zakharov et al., 2019; Zakharova et al., 2019), while the analysis based on the ALOS-2 PALSAR-2 data was performed in (Bondur et al., 2019).

SELECTION OF THE RESEARCH METHOD

Properties of the interaction of radio waves with complex surface structures resulting in multiple rereflections or having spatial anisotropy can be identified using polarization measurements. Such measurements are provided by polarimetric SAR, which radiates, for example, linearly polarized waves with vertical (V) and horizontal (H) polarizations and receives the reflected signal at copolarized (VV and HH signals) and cross-polarized (VH and HV) channels. This multichannel polarimetric operation of the radar significantly increases the information content of measurements (Cloude, 2010; Lee and Pottier, 2009).

The result of measurements using polarimetric SAR is the scattering matrix

$$[S] = \begin{bmatrix} S_{HH} & S_{HV} \\ S_{VH} & S_{VV} \end{bmatrix}. \qquad (1)$$

Here, S_{ij}, are complex scattering coefficients for radiation with j polarization and reception with i polarization.

The physical basis of radar polarimetry methods is the dependence of the polarization state of the radar signal on the backscattering mechanism of radio waves by terrestrial objects. Various transformations of the scattering matrix make it possible to reveal these mechanisms and thereby identify various objects. Note that condition $S_{HV} = S_{VH}$ is satisfied for monostatic sensing.

The authors of (Czuchlewski et al., 2003) used an aircraft polarimetric SAR of the L band to determine the changes in surface reflective properties caused by a landslide after an earthquake in Taiwan. Decomposition of the surface scattering matrix using the Cloude–Pottier method (Cloude and Pottier, 1997) made it possible to determine the nature of changes in the mechanisms of scattering of the Earth's surface due to a landslide. It was noted that the SAR images obtained at one polarization are insufficient for identifying and mapping landslides.

In the publication by (Yonezawa et al., 2012), the authors used polarimetric data from the PALSAR L-band satellite to detect landslides caused by the earthquake in Japan in 2008. The contribution of various scattering mechanisms on the surface of landslide areas was studied using the Freeman–Durden (1998) and Cloude–Pottier decomposition methods. According to the Freeman–Durden decomposition data, the surface scattering component prevails in the areas affected by large-scale landslides. Cloude–Pottier decomposition parameters such as entropy H, anisotropy A, and angle α were also calculated for landslide areas.

An automatic classification based on the segmentation of these parameters on the H-α plane uniquely distinguishes landslide regions from other objects such as forest, water, and snowy areas, but it is ineffective when there is agricultural land within the radar image. The landslide area is difficult to identify in a single-channel image; at the same time, it is confidently recognized when analyzing polarimetric images. It was found that, when detecting landslide zones, polarimetric images with a resolution of 30 m are more informative than single-channel images with a resolution of 10 m.

The efficiency of using of polarimetric multifrequency SARs for detecting landslide zones in forested mountains was assessed in (Shimada et al., 2014). The results show that X-band SARs are less efficient in detecting landslides, since the penetration of waves in this band through the forest layer is worse than in the L-band.

The X-band polarimetric response of landslide zones has also been studied using a high-resolution aircraft SAR system in China (Li et al., 2014a). Polarimetric expansions including the Yamaguchi quaternary decomposition (Yamaguchi et al., 2005) and the Cloude–Pottier decomposition were used to analyze the dispersal mechanisms of several landslides in 2008 caused by the earthquake in southwestern China. Experimental X-band data show that areas subjected to large-scale landslides are characterized by a mixture of surface, double, and volumetric scattering. The results of the classification are also presented, which are based on the controlled parameters of the Wishart classifier (Ferro-Famil et al., 2001) and on the parameters of the similarity of polarimetric scattering, which make it possible to clearly distinguish landslide areas from other types of surfaces, such as forest and water.

The authors of (Li et al., 2014b) used sets of radar images obtained using a fully polarimetric onboard high-resolution synthetic aperture X-band radar system. The Pauli decomposition elements resulting from the scattering matrix transformation were combined into an RGB pseudocolor and converted to the hue-saturation-intensity color space (HSI). Then, a combination of k-means clustering and HSI images from different channels was used step by step to automatically isolate landslide zones.

The authors of (Luo et al., 2015) discuss a method for identifying landslides based on the methods of polarimetric decomposition of C-band data obtained before and after the landslide, followed by the use of the Wishart classifier (Ferro-Famil et al., 2001). An analysis of the polarimetric signatures of the three landslides caused by the 2008 China earthquake shows that the dominant signal scattering mechanism by landslides is the surface scattering component with a scattering entropy between 0.6 and 0.8. The territories adjacent to the landslide are characterized by the dominance of volumetric scattering, while the scattering entropy is almost similar to the entropy in landslide areas. By comparing the location of the surface scattering areas in the image after the event with the volumetric scattering areas in the image before the event and combining the scattering entropy maps, it is possible to estimate the recognition errors of landslide zones.

The results in (Shibayama et al., 2015) are devoted to the dependence of the polarimetric indices for landslides under forest cover on the local angle of incidence of the radio wave. When studying the reflective properties of the landslide surface, the data from the PolSAR sensor were used, which carried out surveys from different directions. It turned out that the scattering power and the polarimetric correlation coefficient of landslides significantly decrease with the local angle of incidence, while these indicators do not change for the surrounding forest. This fact leads to the development of a method for the efficient detection of a landslide zone using polarimetric information.

Polarimetric images of the Pi-SAR-L2 aircraft radar (Watanabe et al., 2016) were analyzed to find out the optimal parameters of the complete polarimetric L-band survey and the viewing angle for detecting the landslide zone. They were obtained from four different directions of the landslide zone survey on Izu Oshima Island triggered by the typhoon on October 16, 2013. Multiple polarimetric parameters, including the backscatter coefficient, coherence between two polarimetric states, quaternary decomposition parameters (double reflection/bulk/surface/helical scattering), and eigenvalue decomposition parameters (entropy/alpha/anisotropy), were calculated to detect landslide areas. Radar sensing of the forward (closest to the radar) slope was more preferable for identifying a landslide, while observations from the opposite side were less informative, indicating that a smaller local angle of incidence provides a better distinction between landslide and forest areas.

The authors of (Wang et al., 2016) suggested a method to assess the displacement of the landslide that allows one to reveal the dynamics of backscattering. The differences between the two Pauli scatter vectors on different dates were estimated, which made it possible to estimate the displacement of the landslide surface in the southwestern part of the state of Colorado, United States.

Most of the SAR-based approaches to landslide detection described in the literature use very high resolution (VHR) data, provided that the survey was carried out shortly before the landslide event, which is quite rare. Modern VHR SAR missions such as Radarsat-2, TerraSAR-X, or COSMO-SkyMed do not systematically cover the entire Earth's surface due to various constraints. Therefore, a method for mapping landslides is presented in (Plank et al., 2016), which is based on detecting changes between optical images before the event and the polarimetric entropy obtained from the polarimetric SAR data after the event. As a rule, information about the state of the surface before the event is available from high-resolution optical images of Landsat-8 or Sentinel-2, which systematically survey all of the Earth's land.

In this work, to analyze landslide processes using the example of the collapse of the slope of the bank of the Bureya River, we will use two of the most widely used methods for analyzing polarization radar images based on the decomposition of the scattering matrix: the one based on the physical model, the Freeman–Durden decomposition (Freeman and Durden, 1998), and the mathematical model using the eigenvalues and eigenvectors of the coherence matrix (Cloude–Pottier decomposition) (Cloude and Pottier, 1997). These methods were used not only to study landslide areas, but also to study the surrounding area, including forest, river ice cover, etc. PolSARpro software was used to analyze polarimetric data (PolSARpro, 2019).

ANALYSIS OF DECOMPOSITIONS OF POLARIMETRIC SIGNALS

The Freeman–Durden decomposition (Freeman, Durden, 1998) is based on a three-component power dissipation matrix model. In this case, the total backscattering power P is assumed to consist of the sum of three independent terms: the power of single (surface) scattering, the power of the echo signal that has undergone a double rereflection by structures similar to a dihedral corner reflector, and the power of volumetric (multiple) scattering

$$P = |S_{HH}|^2 + 2|S_{HV}|^2 + |S_{VV}|^2 = P_s + P_d + P_v, \qquad (2)$$

where subscripts s, d, and v denote surface, double, and volumetric scattering, respectively.

Single surface scattering is a typical scattering mechanism from land or water. Double reflections occur when there are vertically oriented targets on a horizontal surface; it is often found in built-up areas (reflections from the ground and walls), as well as in forests (reflections from trunks and ground). Volumetric scattering occurs when there is a layer of randomly oriented elementary reflectors, for example, tree branches.

The model uses the correlation between the elements of the scattering matrix (1), described by the covariance matrix:

$$\langle C\rangle = \begin{bmatrix} \left\langle |S_{HH}|^2 \right\rangle & \left\langle \sqrt{2} S_{HH} S_{HV}^* \right\rangle & \left\langle S_{HH} S_{VV}^* \right\rangle \\ \left\langle \sqrt{2} S_{HV} S_{HH}^* \right\rangle & \langle 2|S_{HV}|\rangle & \left\langle \sqrt{2} S_{HV} S_{VV}^* \right\rangle \\ \left\langle S_{VV} S_{HH}^* \right\rangle & \left\langle \sqrt{2} S_{VV} S_{HV}^* \right\rangle & \left\langle |S_{VV}|^2 \right\rangle \end{bmatrix}. \qquad (3)$$

The model assumes that the correlated and transversal components of the scattering matrix (1) are not statistically correlated:

$$\left\langle S_{HH}S_{HV}^{*}\right\rangle \simeq \left\langle S_{VV}S_{HV}^{*}\right\rangle \simeq 0,$$

and, moreover, it assumes symmetry of the matrix $S_{HV} = S_{VH}$ (therefore, the dimension of the covariance matrix is 3 × 3, not 4 × 4).

A number of assumptions separately associated with each of the scattering mechanisms are also used, such as the uniform distribution of the orientation of the elementary reflectors of the dipoles in the bulk layer, the applicability of the Bragg model to the surface component of scattering, and the diagonality of the scattering matrix characterizing double rereflection. After parameterizing the elements of the scattering matrix for each of the three mechanisms using the named constraints, a set of equations is obtained:

$$\begin{gathered}\left\langle |S_{HH}|^{2}\right\rangle = |b|^{2} f_s + |a|^{2} f_d + f_v,\\ \left\langle |S_{HV}|^{2}\right\rangle = \frac{f_v}{3},\\ \left\langle |S_{VV}|^{2}\right\rangle = f_s + f_d + f_v,\\ \left\langle S_{HH}S_{VV}^{*} = bf_s + af_d + \frac{f_v}{3}\right\rangle,\end{gathered} \tag{4}$$

where f_s, f_d, and f_v are the contributions of the surface, double (dihedral), and volumetric scattering, respectively; a and b are the degree of correlation of the horizontal and vertical components for double and surface scattering, respectively.

Thus, there are four equations with five unknowns. The last assumption is introduced in order to obtain a unique solution of the system: depending on the sign of the real part of the $\left\langle S_{HH}S_{VV}^{*}\right\rangle$ component, the dominant scattering mechanism is either the surface (then, $a = -1$) or double (then, $b = 1$).

The model works best under the conditions when the contribution of either surface or double reflections is small. It should be noted that the latter is often the case for natural covers in the L band.

After all the unknowns have been found, the final decomposition of power P into three components P_s, P_d, and P_v is performed from the formulas

$$\begin{gathered}P_s = f_s(1 + |b|^2),\\ P_d = f_d(1 + |a|^2),\\ P_v = \frac{8f_v}{3} = 8\left\langle |S_{HV}|^2\right\rangle.\end{gathered} \tag{5}$$

The Cloude–Pottier decomposition (Cloude and Pottier, 1997) is based on the analysis of the eigenvalues of the coherence matrix, which is obtained for the scattering vector written in the Pauli basis:

$$\mathbf{k}_p = \frac{1}{\sqrt{2}}\begin{bmatrix}S_{HH} + S_{VV}\\ S_{HH} - S_{VV}\\ 2S_{HV}\end{bmatrix}. \tag{6}$$

Here, as in the Freeman–Durden expansion, condition $S_{HV} = S_{VH}$ is assumed to be satisfied. The elements of the coherence matrix [T] show the degree of correlation between the elements of vector $\mathbf{k}_P$:

$$\langle [T]\rangle = \frac{1}{2}\left\langle\begin{bmatrix}(S_{HH}+S_{VV})(S_{HH}+S_{VV})^{*} & (S_{HH}+S_{VV})(S_{HH}-S_{VV})^{*} & 2(S_{HH}+S_{VV})S_{HV}^{*}\\ (S_{HH}-S_{VV})(S_{HH}+S_{VV})^{*} & (S_{HH}-S_{VV})(S_{HH}-S_{VV})^{*} & 2(S_{HH}-S_{VV})S_{HV}^{*}\\ 2S_{HV}(S_{HH}+S_{VV})^{*} & 2S_{HV}(S_{HH}-S_{VV})^{*} & 4S_{HV}S_{HV}^{*}\end{bmatrix}\right\rangle. \tag{7}$$

Since the matrix [7] is self-conjugated, it can be reduced to the diagonal form

$$[T] = [U_3]\begin{bmatrix}\lambda_1 & 0 & 0\\ 0 & \lambda_2 & 0\\ 0 & 0 & \lambda_3\end{bmatrix}\left[U_3^{*T}\right], \tag{8}$$

where $\lambda_1 \geq \lambda_2 \geq \lambda_3$ are the eigenvalues of matrix T, which are real numbers, and the unitary matrix $[U_3]$ consists of its eigenvectors.

The dominant scattering mechanism in the model is the mechanism corresponding to the eigenvector with the maximum eigenvalue λ_1; the other two vectors describe the second and third most frequent scattering mechanisms.

The degree of randomness of scattering is described by the entropy

$$H = \sum_{j=1}^{3} -P_j \log_3 P_j, \tag{9}$$

where P_j is the probability of each of the three mechanisms:

$$P_j = \frac{\lambda_j}{\lambda_1 + \lambda_2 + \lambda_3}. \tag{10}$$

If only one of the eigenvalues of the coherence matrix is nonzero, then, with a probability equal to one, a single scattering mechanism (deterministic case) is observed and $H = 0$.

Table 1. Scheme of the interpretation of the results of classification of H-α

Zone number	Entropy, H	Alpha, α	Scattering mechanism
1	0.9–1.0	55–90	High entropy, double scattering
2	0.9–1.0	40–55	High entropy, dipole scattering
3	0.9–1.0	0–40	High entropy, surface scattering
4	0.5–0.9	50–90	Moderate entropy, double scattering
5	0.5–0.9	40–50	Moderate entropy, volumetric scattering
6	0.5–0.9	0–40	Moderate entropy, surface scattering
7	0–0.5	47.5–90	Low entropy, double scattering
8	0–0.5	42.5–47.5	Low entropy, dipole scattering
9	0–0.5	0–42.5	Low entropy, surface scattering

If, on the other hand, there is no distinguished scattering mechanism and $\lambda_1 = \lambda_2 = \lambda_3$, then $H = 1$.

However, neither of these extreme cases occur in reality; an intermediate variant is usually observed. The case when $\lambda_1 \gg \lambda_2 \cong \lambda_3$ can be considered to some extent an approximation to $H = 0$. A typical example is the Bragg scattering from a rough surface. Approximation to $H = 1$ is scattering by a cloud of chaotically oriented dipoles, which simulates crowns of dense forests. High entropy values usually indicate the presence of vegetation.

Parameter α in the Cloude–Pottier decomposition is calculated as the weighted average

$$\tilde{\alpha} = P_1\alpha_1 + P_2\alpha_2 + P_3\alpha_3, \tag{11}$$

where α_j is one of the angles parameterizing the eigenvector $\mathbf{e}_j$:

$$[e_j] = e^{i\phi_j}\left[\cos\alpha_j \;\; \sin\alpha_j\cos\beta_j e^{i\delta_j} \;\; \sin\alpha_j\sin\beta_j e^{i\gamma_j}\right]^T. \tag{12}$$

Angle α ranges from 0° (which corresponds to the surface scattering mechanism) to 90° (which corresponds to double rereflection from an ideally conducting surface of a dihedral angle).

An intermediate value of 45° corresponds to dipole scattering.

Table 1 and Fig. 1 show the segmentation results with nine zones corresponding to different scattering mechanisms, as well as a diagram with different scattering mechanisms in the H-α plane (Cloude and Pottier, 1997).

RESULTS OF DECOMPOSITION APPLICATION AND DISCUSSION

Application of the Freeman–Durden decomposition. Figure 2 shows orthorectified images of the Freeman–Durden decomposition parameters based on the ALOS-2 PALSAR-2 polarimetric data on November 28, 2018, before the event associated with the landslide and images on December 12, 2018, after the collapse of the hill slope. The contributions of the scattering mechanisms correspond to the brightness of the RGB channels of the pseudocolor synthetic image: double reflection is transmitted in red, volumetric scattering is shown in green, and surface scattering is in blue.

The predominance of red hues indicates the presence of double reflection; this is typical for a rare forest with trunks, the thickness of which is comparable with the wavelength, as well as for steep shores and structures with vertical edges. Volumetric scattering dominates in the reflection from a set of tree crown branches in the forest cover; however, the forest also contains structures with a double (surface–tree trunk) scattering mechanism. Surface scattering (blue) and specular reflection from a smooth surface (dark tone) are observed on the water surface of the Bureya River in the period before freezing and landslide. Different shades of blue are found in relatively flat areas, the small-scale roughness of which is generally smaller than the wavelength. White indicates the equal contribution of all three components.

Let us consider the dynamics of the components of the Freeman–Durden decomposition for the following regions shown in Fig. 3:

(1) Region 1, an elevation of landslide masses in the riverbed like on December 12, 2018;

(2) Region 2, an impact zone of the water–ice "tsunami";

(3) Region 3, the surface of the Bureya River (water on November 28, 2018; ice cover on December 12, 2018);

(4) Region 4, the zone of collapse of the slope of the hill.

One peculiar feature of this landslide was that about 18 million m^3 of landslide masses (Zakharova et al., 2019) ended up in the riverbed and formed an elevation that blocked the river (Region 1).

Table 2 presents the percentage ratios of the contribution of each component to the radar backscatter before and after the collapse of the hill slope for a

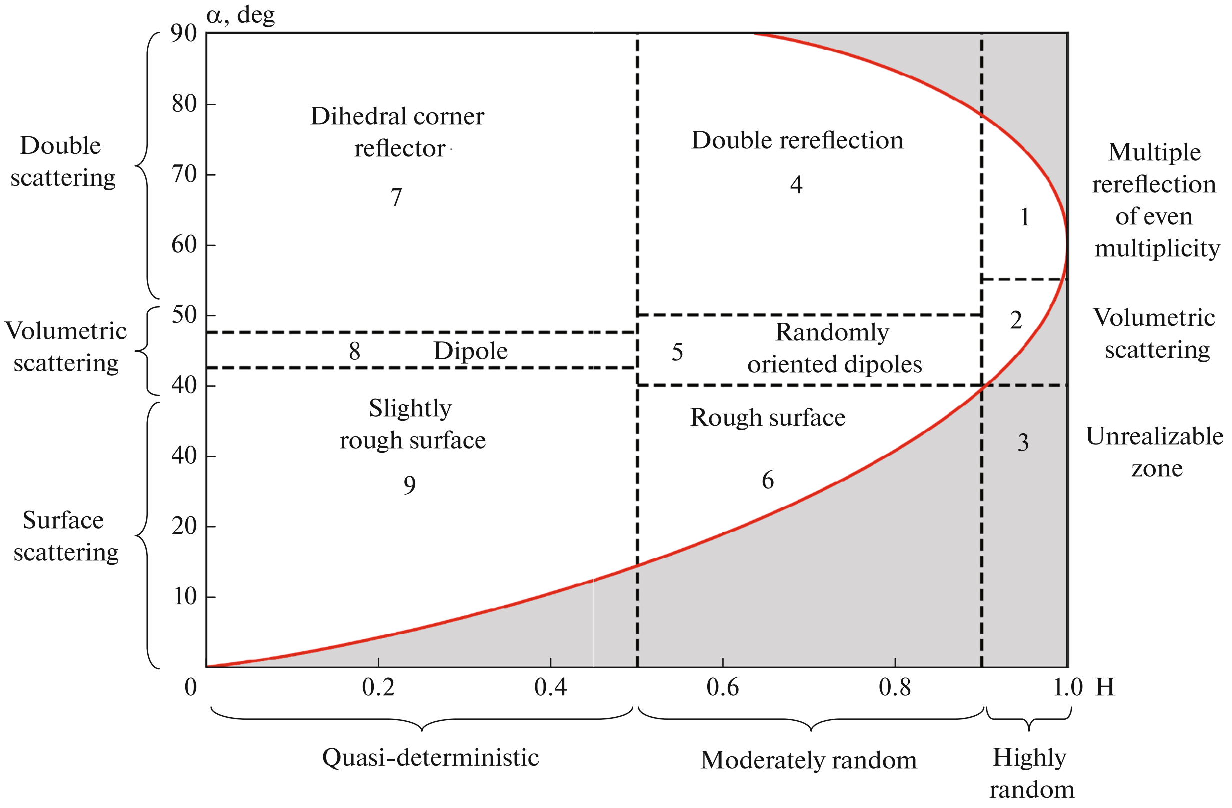

Fig. 1. Location of zones with different scattering mechanisms on the H-α plane.

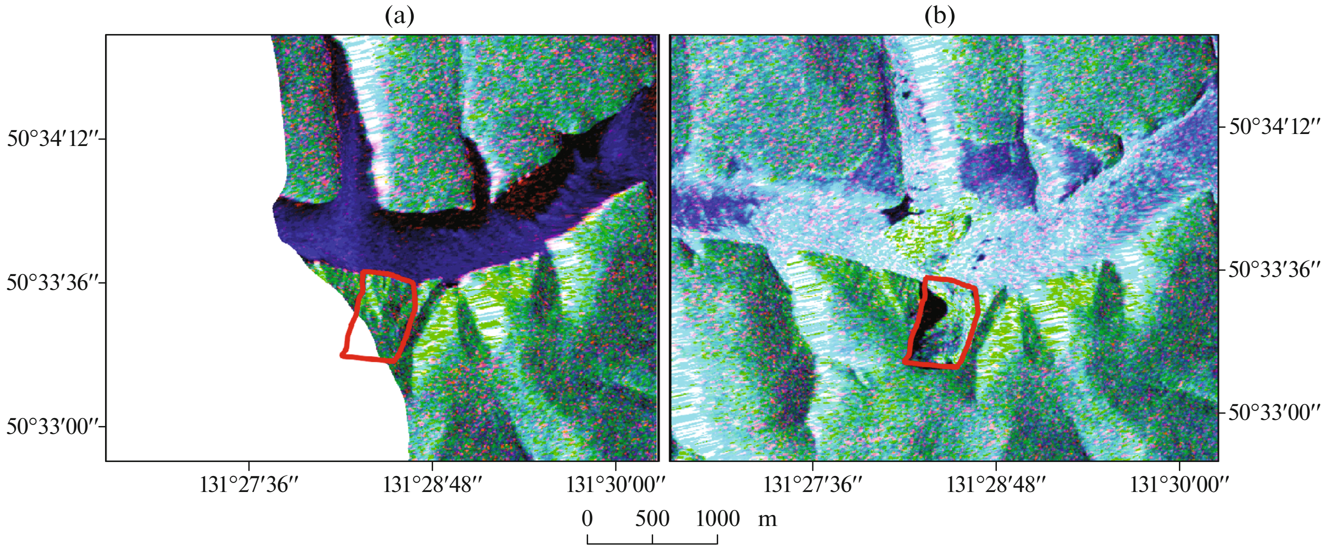

Fig. 2. Freeman–Durden decomposition: data on November 28, 2018 (before the event) (a), data on December 12, 2018 (after the event) (b).

quantitative assessment of the change in reflective characteristics. Hence, a change in the dominant physical mechanism of radar backscattering is characteristic of contour 1, which covers part of the coastal zone before collapse.

An analysis of Table 2 shows that, before the event associated with the landslide on November 28, 2018, backscatter contained 49.7% of single scattering from the “rough” water surface in the river and 45.1% of volumetric scattering. After the collapse on December 12,

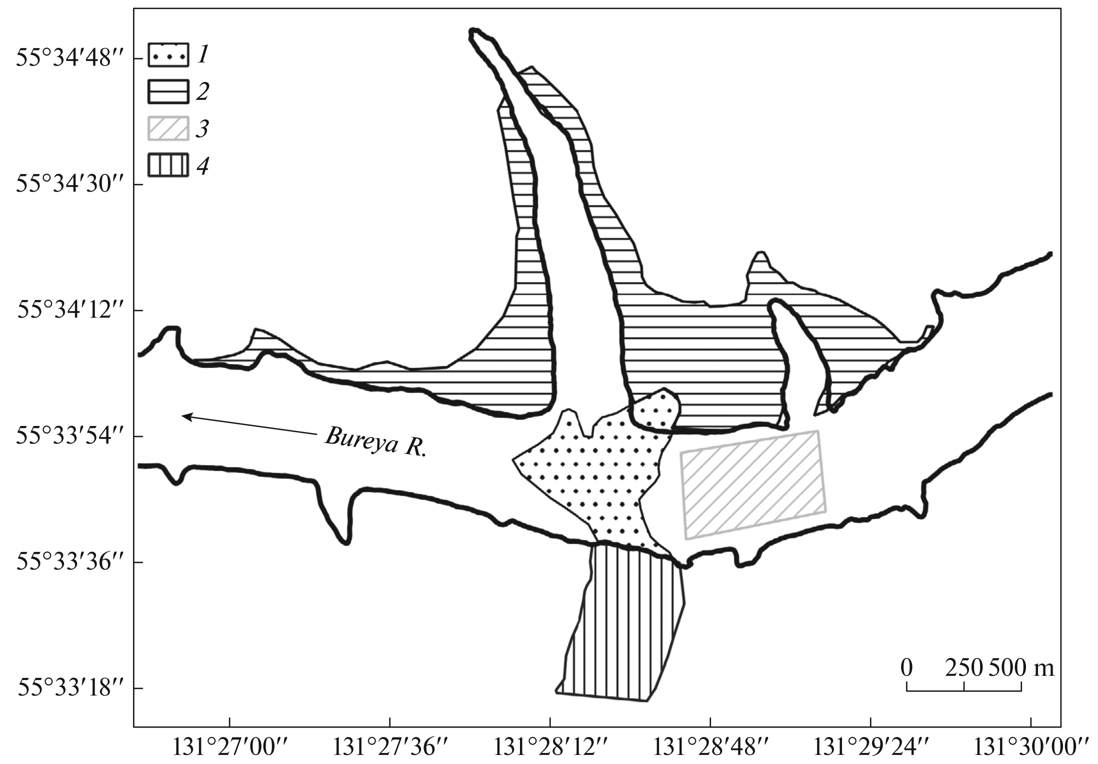

Fig. 3. Scheme of the slope collapse zone.

2018, the volumetric scattering by the surface of the landslide topside began to amount to 62.1% while single scattering was 36.3%. Such a ratio indicates significant depolarization, which may be due to the rereflection of the radar echo signal from a pile of randomly oriented large and small stones, along with patches of surviving tree vegetation.

Horizontally shaded Region 2 corresponds to a fragment of the Earth's surface which was covered with forest vegetation before the landslide; this is consistent with the fact of volumetric scattering (58.5%) in this area according to the radar polarimetry data on November 28, 2018. After a large-scale collapse of part of the coastal hill and ice tsunami, the previously dominating mechanism of volumetric scattering gave way to single scattering (60.5%). Such a change in the dominant scattering mechanism indicates a change in the type of surface of the Earth: the forest vegetation was completely washed away by the tsunami wave.

Region 3 corresponds to the water–ice cover on the river, for which the percentage of the components of the three-component transformation was also calculated. In this region, an insignificant change in the surface diffuse scattering (from 59.4 to 59.6%) is observed with an increase by 7% in the volumetric scattering mechanism (from 31.7 to 38.5%) and a decrease by the same amount of double scattering (from 8.9 to 1.9%). The latter may mean a transition from the inhomogeneities of the wind waves on the river water surface on November 28, 2018, which are to some extent characterized by double reflection, to

Table 2. Distribution of the components of the Freeman–Durden decomposition before (November 28, 2018) and after the landslide (December 12, 2018)

Number of region	November 28, 2018			December 12, 2018		
	P_d, %	P_v, %	P_s, %	P_d, %	P_v, %	P_s, %
Region 1	5.2	45.1	49.7	1.6	62.1	36.3
Region 2	2.8	58.5	38.7	1.7	37.8	60.5
Region 3	8.9	31.7	59.4	1.9	38.5	59.6
Region 4	2.6	84.1	13.3	2.1	71.2	26.7

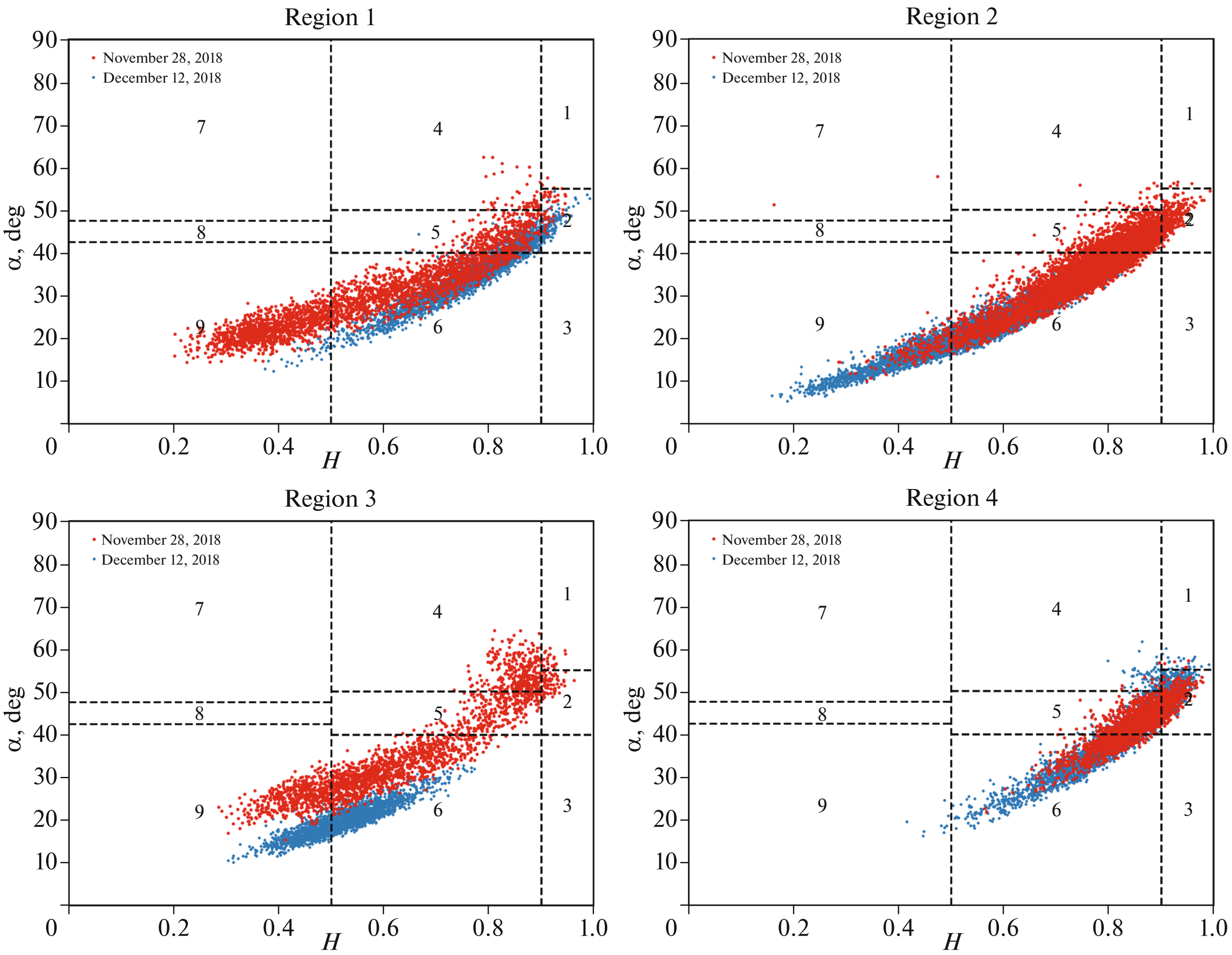

Fig. 4. Results of H-α decomposition: before the descent of the landslide in red and after the event in blue.

randomly oriented linear reflectors (tree fragments, cracked ice) on the surface of the ice cover.

Before the landslide event, Region 4 was represented by forest cover with a corresponding dominance of the volumetric scattering component (84.1%). After the descent of the landslide, despite the absence of trees, the volumetric scattering becomes smaller by 13%, but remains dominant. Similarly to Region 1, this effect can be interpreted by the presence of chaotically oriented scatterers (as well as randomly located in space small-scale inhomogeneities of the relief and piles of trees), acting like volumetric inhomogeneities. An increase in surface scattering by more than 13% means the appearance of rough surfaces after the landslide with irregularities of the order of the radio wave length.

Note that more visual additional information in the form of color images can be found on the web page (Landslide on the Bureya River, 2019) in the “Polarimetric composite” layer.

Decomposition *H*-α. Figure 4 shows the results of the decomposition of scattering mechanisms on the H-α plane constructed using the Cloude–Pottier method in different test sites before and after the landslide.

The Cloude–Pottier method allows one to reveal the main scattering mechanism, which can be one of nine types (see Table 1). The types are distinguished according to the values of parametric angle α from 0° to 40°–42°, which correspond to the surface type of scattering; those from 40°–42° to 50°–55° are related to dipole scattering and those exceeding 55° are related to double reflection. Surface scattering is classified into two types with high and moderate entropy. On the terrain, this usually reflects the level of fine-scale roughness of the reflective surface. Dipole scattering corresponding to the volumetric type of scattering in the Freeman–Durden expansion is subdivided into three types (with low, moderate, and high entropy).

The double scattering mechanism is similarly subdivided into three types according to the level of entropy.

The results shown in Fig. 4 indicate that the descent of the landslide changed the values of entropy *H* and angle α to one degree or another; however, in different regions these changes were of different nature. In Regions 1 and 3, after the descent of the landslide, the values of *H* and α began to occupy a noticeably more compact area. In all regions, either entropy *H* or the values of α decreased after the descent of the landslide, which indicates a tendency to smooth the reflecting surface. Let us analyze the changes in each region separately.

Region 1 before the landslide was the water surface of the river with a small area of the wooded bank, and after the landslide it became the surface of the landslide soil that blocked the river bed. It is seen from Fig. 4 that, after the event associated with the descent of the landslide, there was a decrease in the values of entropy *H* with a simultaneous decrease in α in this region. Thus, the values of *H* before the landslide were in the range 0.2–0.95 and, after its descent, they appeared in the range 0.4–0.95; the values of α, respectively, were in the range 15°–60°, and after the landslide they took the value 12°–50°.

According to the segmentation of the *H*-α plane into nine zones (see Fig. 1), we find that, before the landslide, parameters *H* and α were located mainly in zones 6 and 9, which are characteristic of surface scattering, as would be expected for the water surface. However, some of the points are located in zones 2, 4, and 5, which are typical for multiple (volumetric) scattering characteristic of vegetation. Apparently, this can be explained by the strong wind waves at the water surface at the time of the survey, as well as by a fragment of the shore opposite to the landslide, which fell into the boundaries of section 1 due to the fact that it was covered with descended ground. After the event, Region 1 became a landslide surface formed by ground and rock debris of various sizes interspersed with fallen trees. The decomposition results show that in this case the Bragg scattering practically disappears, and most of the echo signal comes from large-scale irregularities, which also form multiple scattering characteristic of segmentation zones 2 and 5.

Region 2 corresponds to the initially sloping almost flat coast with forest cover, which was washed away by a water–ice wave of the tsunami type. It follows from the results of the *H*-α classification that scattering by the surface of Region 2 is surface scattering (zones 6 and 9) and scattering from vegetation (zones 5 and 2) before the landslide; after the landslide the scattering is mainly surface with an increase in the proportion of the Bragg scattering.

Region 3 on the surface of the river is free from landslide effects. The difference in the conditions of radar surveys before and after the landslide is that, on the day of the first survey, the river was not frozen yet and the ice cover appeared on the second day. It follows from the data shown in Fig. 4 that the ranges of *H* and α on the water surface and ice cover almost do not intersect. In the case of the water surface, multiple scattering in zones 2, 4, and 5 indicates that the water surface of the river was likely rough during the survey period, as well as in Region 1. The backscatter of the ice cover after freezing is single surface scattering.

Region 4 is actually a landslide slope of a wooded river bank before the descent of landslide masses, as well as a landslide circus that was formed later. It should be noted that the upper (right) part of the point cloud falling into zones 2 and 5, which characterizes volume scattering, almost did not change. This indicates that after the landslide there were many fallen trees, and there is a large amount of soil and fragments of rock, which determine the nature of multiple scattering, similar to the crowns of trees in a forest. It follows from Fig. 4 that, as expected, after the descent of the landslide, the proportion of surface scattering increased.

CONCLUSIONS

A comparison of the results of the Freeman–Durden and Cloude–Pottier decompositions demonstrated their general agreement, but some differences are also observed. They appear, for example, when comparing scattering mechanisms on the surface of a river (Region 3). Thus, the values characterizing the scattering mechanisms based on the Freeman–Durden transformation before the landslide (water surface of the river) and after (ice cover) are quite close: the surface scattering component remained almost unchanged. It was 59.4% and became 59.6%. The volume scattering was 51.7%, and it changed to 58.5%. The contribution of double angular scattering changed most strongly: it decreased from 8.9 to 1.9%.

An analysis of the results based on the Cloude–Pottier classification method shows more significant changes in the scattering mechanisms: after the descent of the landslide, both entropy *H* and the values of angle α decreased notably. Before the landslide there was a notable fraction of volumetric (multiple) scattering, but after the landslide the scattering became purely of the surface type.

In general, the analysis shows that the methods of polarimetric decomposition are efficient and make it possible to reliably identify the changes in the scattering mechanisms that occur as a result of landslides and thereby determine various zones formed during landslides.

ACKNOWLEDGMENTS

We are grateful to the Japan Aerospace Exploration Agency (JAXA) for the ALOS-2 PALSAR-2 radar data provided within the ALOS-2 RA-6 projects (PI 3402 and PI 3092).

FUNDING

This work was performed as part of the framework of state assignments of the Institute of Physical Materials Science, Siberian Branch, Russian Academy of Sciences; the Kotelnikov Institute of Radioengineering and Electronics, Russian Academy of Sciences; and AEROCOSMOS Research Institute for Aerospace Monitoring.

REFERENCES

Akopian, S.Ts., Bondur, V.G., and Rogozhin, E.A., Technology for monitoring and forecasting strong earthquakes in Russia with the use of the seismic entropy method, *Izv., Phys. Solid Earth,* 2017, vol. 53, no. 1, pp. 32–51. https://doi.org/10.1134/S1069351317010025

Bondur, V.G., Zakharova, L.N., Zakharov, A.I., et al., Long-term monitoring of the landslide process on Bureya riverbank based on interferometric L-band radar data, *Sovr. Probl. Dist. Zond. Zemli Kosm.* 2019, vol. 16, no. 5, pp. 113–119. https://doi.org/10.21046/2070-7401-2019-16-5-113-119

Bondur, V.G., Chimitdorzhiev, T.N., Dmitriev, A.V., and Dagurov, P.N., Spatial anisotropy assessment of the forest vegetation heterogeneity at different azimuth angles of radar polarimetric sensing, *Izv., Atmos. Oceanic Phys.*, 2019, vol. 55, no. 9, pp. 926–934. https://doi.org/10.1134/S0001433819090093

Bondur, V.G. and Starchenkov, S.A., Methods and programs for aerospace imagery processing and classification, *Izv. Vyssh. Uchebn. Zaved., Geod. Aerofotos'emka,* 2001, no. 3, pp. 118–143.

Bondur, V.G. and Smirnov, V.M., Method for monitoring seismically hazardous territories by ionospheric variations recorded by satellite navigation systems, *Dokl., Earth Sci.,* 2005, vol. 403, no. 5, pp. 736–740.

Bondur, V.G. and Zverev, A.T., A method of earthquake forecast based on the lineament analysis of satellite images, *Dokl., Earth Sci.,* 2005, vol. 402, no. 4, pp. 561–567.

Bondur, V.G. and Zverev, A.T., Mechanisms underlying the formation of lineament systems registered in space images during the monitoring of seismic danger areas, *Issled. Zemli Kosmosa,* 2007, no. 1, pp. 47–56.

Bondur, V.G., Garagash, I.A., Gokhberg, M.B., Lapshin, V.M., Nechaev, Yu.V., Steblov, G.M., and Shalimov, S.L., Geomechanical models and ionospheric variations related to strongest earthquakes and weak influence of atmospheric pressure gradients, *Dokl., Earth Sci.,* 2007, vol. 414, no. 4, pp. 666–669.

Bondur, V.G., Pulinets, S.A., and Kim, G.A., Role of variations in galactic cosmic rays in tropical cyclogenesis: evidence of Hurricane Katrina, *Dokl., Earth Sci.,* 2008a, vol. 422, no. 7, pp. 1124–1128. https://doi.org/10.1134/S1028334X08070283

Bondur, V.G. and Chimitdorzhiev, T.N., Texture analysis of radar images of vegetation, *Izv. Vyssh. Uchebn. Zaved., Geod. Aerofotos'emka,* 2008a, no. 5, pp. 9–14.

Bondur, V.G. and Chimitdorzhiev, T.N., Remote sensing of vegetation by optical microwave methods, *Izv. Vyssh. Uchebn. Zaved., Geod. Aerofotos'emka,* 2008b, no. 6, pp. 64–73.

Bondur, V.G., Pulinets, S.A., and Uzunov, D., Ionospheric effect of large-scale atmospheric vortex by the example of hurricane Katrina, *Issled. Zemli. Kosmosa,* 2008b, no. 6, pp. 3–11.

Bondur, V.G., Krapivin, V.F., and Savinykh, *V.P., Monitoring i prognozirovanie prirodnykh katastrof* (Monitoring and Forecasting of Natural Disasters), Moscow: Nauchnyi mir, 2009.

Bondur, V.G., Garagash, I.A., Gokhberg, M.B., Lapshin, V.M., and Nechaev, Yu.V., Connection between variations of the stress-strain state of the Earth's crust and seismic activity: the example of Southern California, *Dokl., Earth Sci.,* 2010, vol. 430, no. 1, pp. 147–150. https://doi.org/10.1134/S1028334X10010320

Bondur, V.G., Aerospace methods and technologies for monitoring oil and gas areas and facilities, *Izv., Atmos. Oceanic Phys.,* 2011, vol. 47, no. 9, pp. 1007–1018. https://doi.org/10.1134/S0001433811090039

Bondur, V.G., Krapivin, V.F., Potapov, I.I., and Soldatov, V.Ju., Natural disasters and the environment, *Probl. Okr. Sredy Prir. Resur.,* 2012, no. 1, pp. 3–160.

Bondur, V.G., Garagash, I.A., and Gokhberg, M.B., Large scale interaction of seismically active tectonic provinces: the example of Southern California, *Dokl., Earth Sci.,* 2016a, vol. 466, no. 2, pp. 183–186. https://doi.org/10.1134/S1028334X16020100

Bondur, V.G., Garagash, I.A., Gokhberg, M.B., and Rodkin, M.V., The evolution of the stress state in Southern California based on the geomechanical model and current seismicity, *Izv., Phys. Solid Earth,* 2016b, vol. 52, no. 1, pp. 117–128. https://doi.org/10.1134/S1069351316010043

Chimitdorzhiev, T.N., Dagurov, P.N., Bykov, M.E., Dmitriev, A.V., and Kirbizhekova, I.I., Comparison of ALOS PALSAR interferometry and field geodetic leveling for marshy soil thaw/freeze monitoring, case study from the Baikal lake region, Russia, *J. Appl. Remote Sens.,* 2016, vol. 10, no. 1, pp. 016006–1–016006–12. https://doi.org/10.1117/1.JRS.10.016006

Cloude, S.R. and Pottier, E., A review of target decomposition theorems in radar polarimetry, *IEEE Trans. Geosci. Remote Sens.*, 1996, vol. 34, no. 2, pp. 498–518. https://doi.org/10.1109/36.485127

Cloude, S.R. and Pottier, E., An entropy based classification scheme for land applications of polarimetric SAR, *IEEE Trans. Geosci. Remote Sens.,* 1997, vol. 35, no. 1, pp. 68–78. https://doi.org/10.1109/36.551935

Cloude, S.R., *Polarisation: Applications in Remote Sensing,* New York: Oxford University Press, 2010.

Czuchlewski, K.R., Weissel, J.K., and Kim, Y., Polarimetric synthetic aperture radar study of the Tsaoling landslide generated by the 1999 Chi-Chi earthquake, Taiwan, *J. Geophys. Res.,* 2003, vol. 108, no. F1, p. 6006. https://doi.org/10.1029/2003JF000037

Dmitriev, A.V., Chimitdorzhiev, T.N., Gusev, M.A., et al., Basic products of Earth imaging by space radars with synthesized aperture, *Issled. Zemli. Kosmosa,* 2014, no. 5, pp. 83–91.

Dubina, B.A., Shamov, B.B., and Plotnikov, B.B., Catastrophic flood in Primorye in August 2018, *Sovr. Probl.*

Dist. Zond. Zemli Kosmosa, 2018, vol. 15, no. 5, pp. 253–256.

Ferro-Famil, L., Pottier, E., and Jong-Sen, L., Unsupervised classification of multifrequency and fully polarimetric SAR images based on the H/A/Alpha-Wishart classifier, *IEEE Trans. Geosci. Remote Sens.,* 2001, vol. 39, no. 11, pp. 2332–2342. https://doi.org/10.1109/36.964969

Freeman, A. and Durden, S.L., A three-component scattering model for polarimetric SAR data, *IEEE Trans. Geosci. Remote Sens.,* 1998, vol. 36, no. 3, pp. 963–973. https://doi.org/10.1109/36.673687

Kramareva, L.S., Lupjan, E.A., Amel'chenko, Ju.A., et al., Observation of the hill collapse zone near the Bureya River on December 11, 2018, *Sovr. Probl. Dist. Zond. Zemli Kosmosa,* 2018, vol. 15, no. 7, pp. 266–271. http://omdoki.nextgis.com/resource/103/display

Lee, J.S., Grunes, M.R., and de Grandi, G., Polarimetric SAR speckle filtering and its implication for classification, *IEEE Trans. Geosci. Remote Sens.,* 1999, vol. 37, no. 5, pp. 2363–2373. https://doi.org/10.1109/36.789635

Lee, J.-S. and Pottier, E., *Polarimetric Radar Imaging: from Basics to Applications,* New York: CRC Press, 2009.

Li, N., Wang, R., Deng, Y., Liu, Y., Li, B., Wang, C., and Balzc, T., Unsupervised polarimetric synthetic aperture radar classification of large-scale landslides caused by Wenchuan earthquake in hue-saturation-intensity color space, *J. Appl. Remote Sens.,* 2014a, vol. 8, no. 1, pp. 083595-1–083595-8. https://doi.org/10.1117/1.JRS.8.083595

Li, N., Wang, R., Deng, Y., Liu, Y., Wang, C., Balz, T., and Li, B., Polarimetric response of landslides at X-band following the Wenchuan earthquake, *IEEE Geosci. Remote Sens. Lett.,* 2014b, vol. 11, no. 10, pp. 1722–1726. https://doi.org/10.1109/LGRS.2014.2306820

Luo, S., Tong, L., Chen, Y., and Tan, L., Landslides identification based on polarimetric decomposition techniques using radarsat-2 polarimetric images, *Int. J. Remote Sens.,* 2016, vol. 37, no. 12, pp. 2831–2843. https://doi.org/10.1080/01431161.2015.1041620

Mihajlov, V.O., Kiseleva, E.A., Smol'janinova, E.I., et al., Some problems of landslide processes monitoring using satellite radar images with different wavelengths on the example of two landslides in the Great Sochi, *Fiz. Zemli,* 2014, no. 4, pp. 120–130.

Plank, S., Twele, A., and Martinis, S., Landslide mapping in vegetated areas using change detection based on optical and polarimetric SAR data, *Remote Sens.,* 2016, vol. 8, no. 4, p. 307. https://earth.esa.int/web/polsarpro https://doi.org/10.3390/rs8040307PolSARpro

Shibayama, T., Yamaguchi, Y., and Yamada, H., Polarimetric scattering properties of landslides in forested areas and the dependence on the local incidence angle, *Remote Sens.,* 2015, vol. 7, no. 11, pp. 15424–15442. https://doi.org/10.3390/rs71115424

Shimada, M., Watanabe, M., Kawano, N., Ohki, M., Motooka, T., and Wada, Y., Detecting mountainous landslides by sar polarimetry: a comparative study using Pi-SAR-L2 and X-band SARs, *Trans. JSASS Aerospace Tech. Jpn.,* 2014, vol. 12, no. 29, pp. 9–15. https://doi.org/10.2322/tastj.12.Pn_9

Shirzaei, M., Burgmann, R., and Fielding, E.J., Applicability of Sentinel-1 Terrain Observation by Progressive Scans multitemporal interferometry for monitoring slow ground motions in the San Francisco Bay Area, *Geophys. Res. Lett.,* 2017, no. 44, pp. 2733–2742. https://doi.org/10.1002/2017GL072663

Verba, V.S., Neronskii, L.B., Osipov, I.G., and Turuk, V.E., *Radiolokatsionnye sistemy zemleobzora kosmicheskogo bazirovaniya* (Space-Based Radar Systems for Earth Observation), Moscow: Radiotekhnika, 2010.

Wang, C., Mao, X., and Wang, Q., Landslide displacement monitoring by a fully polarimetric SAR offset tracking method, *Remote Sens.,* 2016, vol. 8, no. 8, p. 624. https://doi.org/10.3390/ rs8080624

Watanabe, M., Yonezawa, C., Iisaka, J., and Sato, M., ALOS/PALSAR full polarimetric observations of the Iwate–Miyagi Nairiku earthquake of 2008, *Int. J. Remote Sens.,* 2012, vol. 33, no. 4, pp. 1234–1245. https://doi.org/10.1080/01431161.2011.554453

Watanabe, M., Thapa, R.B., and Shimada, M., Pi-SAR-L2 observation of the landslide caused by typhoon Wipha on Izu Oshima Island, *Remote Sens.,* 2016, vol. 8, no. 4, p. 282. https://doi.org/10.3390/rs8040282

Yamaguchi, Y., et al., Four-component scattering model for polarimetric SAR image decomposition, *IEEE Trans. Geosci. Remote Sens.,* 2005, vol. 43, no. 8, pp. 1699–1706. https://doi.org/10.1109/TGRS.2005.852084

Yonezawa, C., Watanabe, M., and Saito, G., Polarimetric decomposition analysis of alos palsar observation data before and after a landslide event, *Remote Sens.,* 2012, vol. 4, no. 8, pp. 2314–2328. https://doi.org/10.3390/rs4082314

Zakharov, A.I., Yakovlev, O.I., and Smirnov, V.M., *Sputnikovyi monitoring Zemli: Radiolokatsionnoe zondirovanie poverhnosti* (Satellite Monitoring of the Earth: Radar Imaging of the Surface, Moscow: Librokom, 2012.

Zakharov, A.I., Zakharova, L.N., and Krasnogorskij, M.G., Landslide activity monitoring by radar interferometry methods using trihedral corner reflectors, *Issled. Zemli Kosmosa,* 2018, no. 3, pp. 80–92.

Zakharova, L.N., Zakharov, A.I., and Mitnik, L.M., First results of the assessment of the landslide consequences on the Bureya River bank using Sentinel-1 radar data, *Sovr. Probl. Dist. Zond. Zemli Kosm.,* 2019, vol. 16, no. 2, pp. 69–74.

Zakharova, L.N. and Zakharov, A.I., Interferometric observation of landslide area dynamics on the Bureya River by means of Sentinel-1 radar data in 2017–2018, *Sovr. Probl. Dist. Zond. Zemli Kosm.,* 2019, vol. 16, no. 2, pp. 273–277.

Translated by E. Morozov